Kent Academic Repository

High-resolution three-dimensional flow measurement through dual-frame light field particle tracking velocimetry

Xiaoyu Zhu (朱效宇),[1] Chuanlong Xu (许传龙),[1,a] Md. Moinul Hossain,[2] Boo Cheong Khoo[3]

[1] National Engineering Research Center of Power Generation Control and Safety, School of Energy and Environment, Southeast University, Nanjing 210096, China

[2] School of Engineering, University of Kent, Canterbury, Kent, CT2 7NT, UK

[3] Department of Mechanical Engineering, National University of Singapore, 119260, Singapore

[a]Authors to whom correspondence should be addressed: *chuanlongxu@seu.edu.cn*

Abstract: . Single-camera light field particle image velocimetry (LF-PIV) shows potential for 3D flow measurements in scenarios with limited optical access but faces challenges of low spatial resolution. To address this issue, we propose a dual-frame light field particle tracking velocimetry (LF-PTV) method that enhances spatial resolution in volumetric velocimetry. This approach combines line-of-sight estimation with a customized deep neural network to reconstruct particle volumes while suppressing elongation artifacts. A gradient-fitting localization technique is employed to pinpoint particle centers, and a motion predictor coupled with a topology feature matching method facilitates accurate trajectory tracking between successive frames. The performance of the dual-frame LF-PTV method is systematically evaluated through numerical simulations of Gaussian vortex flows and experimental measurements of wake flow behind a circular cylinder. Comparative analyses are conducted to benchmark the proposed method against other PTV and conventional LF-PIV techniques. Results indicate that the deep neural network effectively refines coarse line-of-sight reconstructions, significantly reducing particle elongation. The deep neural network reconstruction using a single light field camera (LFC) achieves approximate accuracy with the traditional Simultaneous Multiplicative Algebraic Reconstruction Technique using dual LFCs. The gradient-fitting algorithm can achieve superior particle localization, especially in high-density seeding, by reducing outliers and enhancing coverage. Furthermore, the integration of motion prediction with the topology feature matching approach minimizes tracking errors, yielding superior accuracy and spatial resolution in synthetic vortex flow reconstructions. Experimental results further confirm the method's capability to resolve finer wake flow structures, correcting LF-PIV inaccuracies and delivering a threefold enhancement in spatial resolution.

Keywords: Particle tracking velocimetry, Light field imaging, Spatial resolution, Particle matching, Center localization

Nomenclature

C	Particle seeding density
d_C	Chamfer distance
d_0	Distance from the particle center to the gradient line passing through a point
d_i	Particle diameter in voxel unit
$\boldsymbol{d_{pt}}$	Displacement derived from particle tracking
$\boldsymbol{d_{pi}}$	Dense motion predictor
E_j	Intensity of the jth voxel in the measurement domain
I_v	Size of interrogation volume in PIV cross-correlation analysis
$\boldsymbol{n_0}$	Unit vector along the gradient direction
$n_1, n_2, \ldots, n_n$	N-nearest neighboring particles within a search radius of R
n_{vec}	Number of independent displacement vectors returned by PIV or PTV algorithms
p_i'	Intensity of the ith pixel in the back-projection image
q	Weight coefficient that emphasizes the contribution of non-zero pixels in the total loss function
q_k	Displacement weight coefficient used in calculating distances from point to gradient lines
Q	Flow rate
$r_{i,k}$	Distance feature
$s_{i,j}$	Similarity index to assess the similarity between the topology features of two particles
sp_v	Mean vector spacing
$w_{j,i}$	Weight coefficient that describes intensity contribution of voxel to pixel
$\alpha_{i,k}$	Angle feature
$\varepsilon_{at}, \varepsilon_{rt}$	Angle threshold and distance threshold defined in topology feature matching
χ^2	Cumulative distance from a candidate center point to all the gradient-parallel lines
CR	Connected regions
DNN	Deep neural network
GF	Gradient-fitting
LFI/LFC	Light field image/camera
LoG	Laplacian of Gaussian
LoS	Line of sight
LR	Lagrangian regularization
MART	Multiplicative algebraic reconstruction technique
MLA	Microlens array
NN	Nearest neighbor searching
PIV/PTV	Particle image/tracking velocimetry
SPT	Single particle tracking
TFM	Topology feature matching
TR	Time-resolved
TP, FP, FN	True detection, false positive, and false negative in particle detection

1. Introduction

Volumetric optical velocimetry techniques have seen significant advancements in recent years, enabling detailed characterization of unsteady three-dimensional (3D) flow structures [1,2]. Various techniques have been developed for measuring flow field within a 3D domain, including the multiple plane stereo PIV [3,4], scanning PIV [5,6], holographic PIV [7,8], and tomographic PIV (Tomo-PIV) [9,10]. Among these, Tomo-PIV has emerged as a preferred choice due to its ability to achieve high spatial resolution across extensive measurement domains. A unique characteristic of the Tomo-PIV technique is that it invokes the principle of tomography [11] to retrieve volumetric information from 2D projections. These projections can be captured either from multiple viewpoints using conventional cameras or from a single perspective with a microlens array (MLA)-based light field camera (LFC) [12]. The integration of an MLA in front of the camera sensor allows a LFC to record not only light intensity, as a conventional camera does, but also the directions of light rays [13]. This capability encodes complete 3D spatial information into an image, which can then be reconstructed to visualize the 3D scene [14]. Tomo-PIV using a single LFC (commonly referred to as light field PIV, LF-PIV [15]) presents a promising solution for internal flow measurements or applications where multi-camera setups are infeasible owing to the limited optical access [16].

With the 3D particle distributions reconstructed from two successively captured light field images (LFIs), at least two families of approaches are available to estimate flow velocity: the correlation-based method (referred to as PIV) to extract Eulerian velocities and the tracking-based method (referred to as PTV) to follow Lagrangian trajectories. The fundamental principle of PIV involves dividing the measurement volume into small interrogation volumes and determining local motion by maximizing the cross-correlation of voxel intensities within these volumes [17]. As a statistical approach, PIV considers the overall pattern of particle groups rather than depending on individual particles, thereby providing stable velocity measurements [18]. However, it inevitably introduces the spatial filtering effect, particularly for flow scales smaller than the interrogation volume. This limitation impedes the investigation of fine flow features and causes bias errors in regions with steep velocity gradients, such as in turbulent boundary layers and near-wall areas [19]. Additionally, PIV cannot differentiate between moving and stationary regions, resulting in an averaged velocity that combines both. These flaws can be well overcome by tracking-based methods. PTV traces individual particle trajectories, providing significantly higher spatial resolution in flow measurements. It can also resolve sharp interfaces between moving and stationary regions, overcoming the inherent limitations of PIV. Due to these superiorities, PTV has broad applications in fluid dynamics and related fields, including granular avalanche studies and bird flock investigations [21,22].

The implementation of 3D-PTV involves two key stages: particle center localization and particle matching between successive frames [1]. Several methods have been developed to localize particles with sub-voxel precision. A common idea involves fitting the intensity profile of particles to a Gaussian function using either nonlinear least-squares minimization or maximum-likelihood estimation [23,24]. The Gaussian fitting process can also be linearized and solved analytically by fitting the logarithm of the particle intensity to a quadratic function [25]. This method is effective for regular, spherical particles whose intensity distribution generally follows a Gaussian profile. However, due to the limited depth resolution of the LFC, reconstructed particles often demonstrate elongation along depth and appear as ellipsoids [26]. This elongation effect introduces bias errors in particle localization when using the Gaussian-fitting methods. A similar issue arises with the centroid-based methods [27]. A promising alternative for elongated particle localization is the intensity-gradient-based method [28]. This method leverages the property of radially symmetric intensity distributions in non-spherical particles: any line parallel to the intensity gradient passing through a point intersects the particle center. The center can thus be estimated as the point that minimizes the total distance to all such lines. While the gradient-based method demonstrates high precision in single particle tracking (SPT), its efficacy in densely seeded fields, where neighboring particles and elongation effects introduce significant challenges, remains unverified. To ensure accurate particle detection in dense particle fields, further exploration is required to mitigate elongation effects and develop robust particle localization algorithms capable of handling complex scenarios.

Once center locations are detected, particles are matched across successive frames to construct the motion field. A straightforward criterion to track individual particles is the nearest-neighbor (NN) search [29], where the particle pair with the shortest distance is assumed to be the correct match. Alternative strategies include globally optimized searches and local

feature vector-based approaches [30,31], which are computationally efficient and yield high matching rate at low seeding densities. However, in cases where the mean inter-particle distance is smaller than particle displacement, the likelihood of spurious particle pairings increases significantly [32]. To eliminate ambiguous particle associations, temporal consistency (refers to the assumption that a particle's trajectory is smooth and continuous over time) of particle displacement across multiple frames can be employed [33-35]. While effective, this strategy necessitates time-resolved (TR) measurements, which increase system cost and complexity. Moreover, due to the trade-off between frequency and energy of lasers, TR-PTV often suffers from a low signal-to-noise ratio [36]. An alternative approach to enhance PTV robustness is the incorporation of a predictor-corrector scheme [37,38]. This approach leverages a priori knowledge of the velocity field, typically a coarse estimate derived from correlation-based methods, to guide particle linking. The predictor adjusts the particle distribution in the initial frame to approximate that of the subsequent frame, ensuring that particle displacements remain smaller than the inter-particle distances. The predictor-corrector framework is well-suited for dual-frame scenarios where TR facilities are unavailable. However, its performance is highly dependent on the accuracy of the generated predictor. Studies have shown that reconstruction elongation significantly degrades the accuracy of flow estimation by cross-correlation, particularly in the depth direction. Therefore, the efficacy of LF-PTV incorporating the predictor-corrector scheme must be rigorously evaluated. Moreover, further research into advanced particle tracking methods that yield both accurate and kinematically consistent motion fields is required.

A major limitation of the LF-PIV is its low spatial resolution in 3D flow measurement. While PTV enhances the resolution, it faces challenges associated with dense particle fields and elongated reconstructions, particularly in dual-frame configurations where temporal information is limited. To address these issues, this study proposes a dual-frame LF-PTV approach for high-resolution volumetric velocimetry. The proposed method integrates line-of-sight (LoS) estimation with a customized deep neural network (DNN) to reconstruct 3D particle distributions. A gradient-fitting (GF) localization approach is employed to identify the centers of reconstructed elongated particles. Particle trajectories between successive frames are established using a motion predictor combined with topology-based feature descriptors. Numerical tests of Gaussian vortex reconstructions and experimental measurements on the wake flow around a circular cylinder are carried out to evaluate the performance of the dual-frame LF-PTV. Comparative studies between the proposed approach and other PTV methods, as well as the traditional LF-PIV technique, are conducted. The principle and implementation details of the dual-frame LF-PTV are elaborated, and key findings from both numerical and experimental investigations are presented and discussed.

2. Dual-frame light field particle tracking

An overview of the proposed high-resolution LF-PTV technique is illustrated in Fig. 1. Tracer particles are immersed in the test flow, and their motion is recorded using a LFC operating in the double-trigger mode. Two successive LFIs of the particle fields, captured at time instants t_1 and t_2, are processed through a LoS volumetric reconstruction algorithm to produce an initial coarse estimate of 3D particle distributions (CR_1 and CR_2). These coarse reconstructions are then refined by a DNN model, which eliminates artifacts and generates more accurate 3D particle volumes (FR_1 and FR_2). Following refinement, particle centers are detected through the GF localization method. A cross-correlation analysis is subsequently performed to estimate large-scale particle motion, resulting in a sparse displacement predictor. This sparse predictor is interpolated into a denser motion field, which is used to warp the particle centers at t_1 to new coordinates (FR_1'). Particle pairing between FR_1' and FR_2 is then conducted using a topology-feature matching (TFM) approach, enabling the estimation of particle flow trajectories and displacements. The displacement derived from particle tracking (d_{pt}) is combined with the dense motion predictor (d_{pi}) to generate the final displacement field (d_p). By dividing the final displacement by the time interval between t_1 and t_2, the local velocity at each particle position is obtained. A detailed of three key stages of LF-PTV: volumetric particle reconstruction, particle center localization, and particle tracking are explained in the following sections.
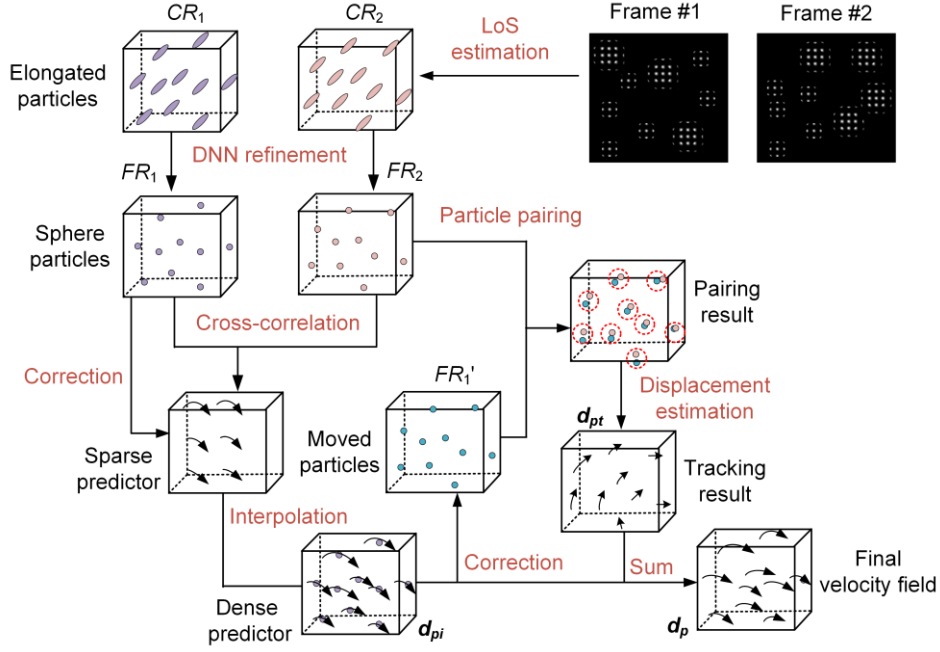
Fig. 1 Overview of proposed dual-frame LF-PTV method: Coarse particle fields are reconstructed by LoS estimation and refined by a DNN model. The final displacement field is a combination of the motion predictor and particle tracking.

2.1 LOS-DNN particle reconstruction

The captured LFIs are used to reconstruct the particle distribution on a 3D voxel grid, where voxel indices and intensities of voxels representing the particle locations are their associated light intensity. This reconstruction is an inverse problem commonly tackled by tomographic reconstruction algorithms, such as the Simultaneous Multiplicative Algebraic Reconstruction Technique (SMART). However, SMART is computationally expensive due to the necessity of calculating weight matrices and iteratively correcting voxel intensities. To enhance reconstruction efficiency, a LoS estimation is employed to generate an initial particle distribution. Due to the unique architecture of the LFC, which incorporates a dense MLA in front of the image sensor, tracing the light rays from the image space back to the object space becomes challenging. Thus, a forward ray tracing method is utilized instead. Specifically, dense rays with different propagation directions are traced from voxels to image pixels using ray transfer matrices [10]. The pixels affected by rays originating from a specific voxel are identified. If a voxel contains tracer particles, its intensity should be greater than zero, and its affected pixels should also exhibit non-zero intensities due to the light contribution from that voxel. Conversely, if some affected pixels have zero intensity, the voxel itself must be a zero-intensity voxel. For instance, as shown in Fig. 2, the voxel J_2 is classified as a zero-intensity voxel, whereas the voxel J_1 is identified as a non-zero voxel that potentially contains particles.
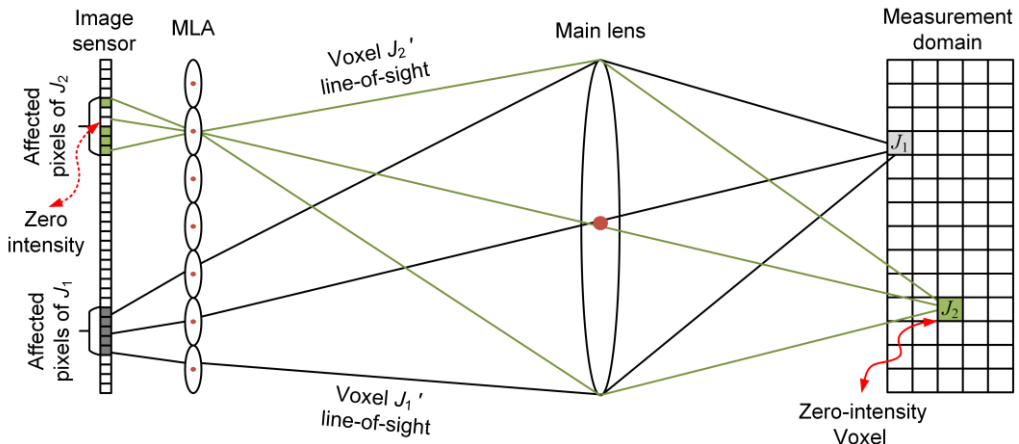

Fig. 2 Principle of volumetric particle reconstruction based on LoS estimation.

Using this classification criterion, dense ray tracing is performed across the measurement domain to estimate a probable

particle distribution. However, the LoS estimation provides only a coarse reconstruction due to uncertainties associated with voxel identification. For instance, in Fig. 2, the intensities of affected pixels of the voxel J_1 may include contributions from neighboring voxels, leading to potential misclassification. Additionally, due to the lower depth resolution of the LFC, reconstructed particles often appear elongated, resembling ellipsoids rather than spheres. To address these issues, a DNN framework is utilized to refine the coarse LoS estimation. This refinement leverages the principle that an accurate particle distribution should produce LF projections that closely match the captured LFIs. Thus, by minimizing the difference between the captured LFIs (p) and the back projections of reconstructed particle volumes (p'), a good estimate of actual particle distribution can be acquired.

The employed DNN model follows a typical 3D U-Net architecture, as illustrated in Fig. 3. The network consists of two primary parts: a contracting path and an expanding path, interconnected via skip connections. In the contracting path, the network progressively reduces the spatial dimensions of the input data while increasing the number of feature channels. This is achieved through 3D convolutional operations that encode the spatial information of the input into multi-channel feature maps. The input to the network is a 3D tensor of size $1\times N_i \times N_j \times N_k$, where $N_i \times N_j \times N_k$ denotes the dimensions of particle volume in units of voxel, and the channel size is one. The contracting path processes this input through a sequence of convolutional layers that extract hierarchical features, followed by max-pooling layers that aggregate key information while reducing spatial resolution. A Sigmoid-weighted linear unit (Swish) is utilized as the activation function, normalizing outputs within the range of 0 to 1. The expanding path mirrors the architecture of the contracting path, progressively increasing the spatial dimensions through up-convolutions. Up-sampling operations are employed to recover the spatial resolution lost in down-sampling. Skip connections are implemented between corresponding layers in the contracting and expanding paths, allowing fine-grained details and spatial information from earlier layers to be preserved and reused. Ultimately, the expanding path restores the spatial resolution, producing a final output that matches the size of the input.
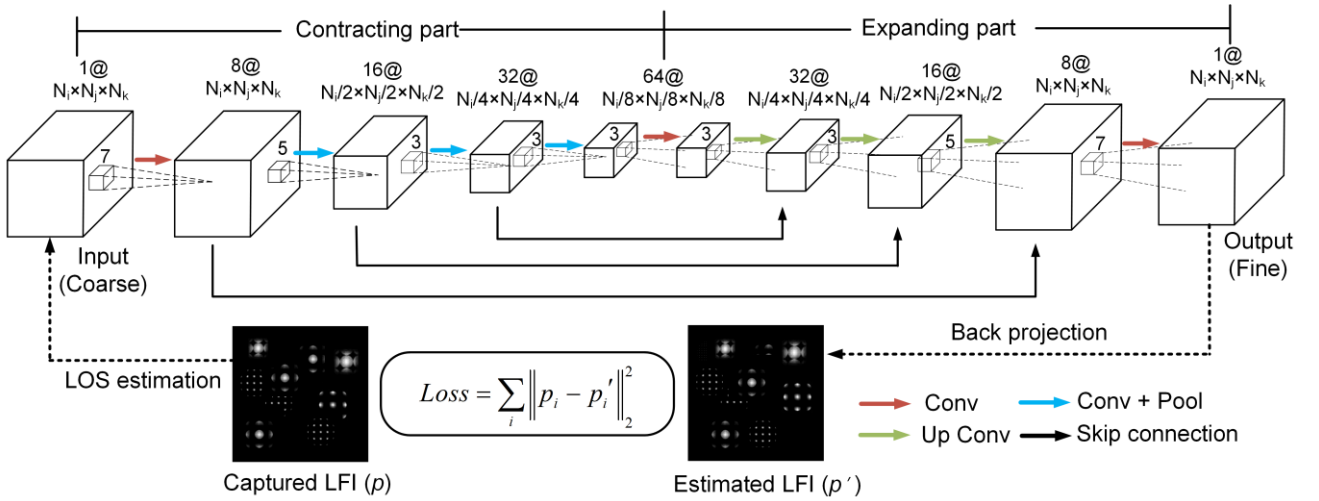

Fig. 3 Structure of DNN used to refine coarse particle distribution estimation by LoS.

The fine-tuned output from the network is projected to the image space, and the resulting back-projection is compared with the captured image to compute the loss. The back-projection process can be expressed as,

$$p_i' = \sum_{j=1}^{N} w_{j,i} E_j \tag{1}$$

where p_i' denotes the intensity of the i_{th} pixel in the back-projection image, E_j is the intensity of the j_{th} voxel in the measurement domain, and $w_{j,i}$ describes the intensity contribution of the voxel j to pixel i, which can be experimentally calibrated [45,46], Here, N denotes the number of voxels that have intensity contribution to the pixel. The loss function of the network is defined as

$$Loss = q\sum_{in}\left\| p_{in} - p_{in}' \right\|_2^2 + \sum_{iz}\left\| p_{iz} - p_{iz}' \right\|_2^2 \tag{2}$$

where p_{in} and p_{iz} refer to the intensity of non-zero-intensity pixels and zero-intensity pixels, respectively, and q is a weight coefficient used to describe the contribution of non-zero pixels in the loss function. The training process aims to minimize the squared differences between the estimated and the captured LFIs, ensuring the final output approximates the actual particle distributions. Unlike supervised deep learning networks, which depend heavily on the quality of the training dataset, the employed DNN adopts an unsupervised learning strategy. This approach eliminates the dependency on labeled data, enhancing the model's generalization ability [47,48].

2.2 Gradient-based particle center detection

The particle volumes that contain 3D particle distributions are reconstructed by the LoS and the DNN, and a GF localization method is utilized to identify the centers of particles. This method exploits the property of symmetric intensity distributions, where any line passing through a point and parallel to the gradient at that point will intersect the particle center (detailed below). Thus, the particle center can be estimated as the point that minimizes the cumulative distance to all gradient-parallel lines. The gradient-fitting localization process, illustrated in Fig. 4, involves the following steps:
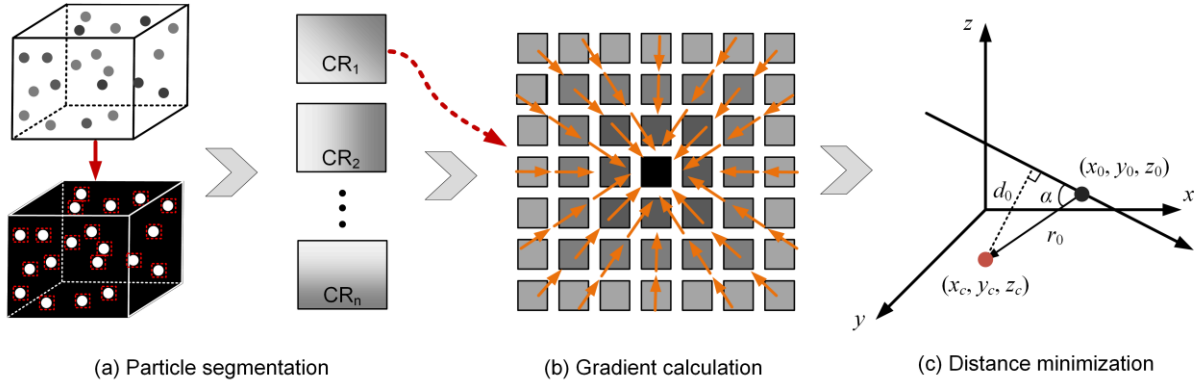

(a) Particle segmentation   (b) Gradient calculation   (c) Distance minimization

Fig. 4 Flowchart of GF method for particle center localization.

(*i*) *Particle segmentation*: The method starts by converting the DNN output to a 3D binary image. This requires an adaptive intensity threshold to segment particles from the background. In this binary image, adjacent voxels with an intensity value of 1 are grouped into connected regions (CRs), each assumed to represent a single particle. Morphological operations are used to delineate the CR, and the intensity distribution within each CR is extracted from the grayscale image to create feature maps.

(*ii*) *Gradient calculation*: For each feature map, the intensity gradient at each discrete voxel location is computed. The gradient indicates the direction and rate of intensity variation, pointing from lower to higher intensity regions. For particles with an approximately radial symmetric intensity distribution, the gradient vectors ideally converge toward the particle center, as illustrated in Fig. 4(b).

(*iii*) *Distance minimization*: At each gradient point, a line is drawn parallel to the gradient direction. In an ideal scenario, these lines intersect at a common point representing the true particle. However, due to noise and reconstruction artifacts in the voxel-based 3D image, these lines instead form a cluster of intersections near the true center. For an arbitrary point (x_0, y_0, z_0) in the gradient field [Fig. 4(c)], there is a distance (d_0) from the particle center (x_c, y_c, z_c) to the gradient line passing through this point, which can be computed as

$$d_0{}^2 = \left|\vec{r}_0\right|^2 - \left(\left|\vec{r}_0\right|\cos\alpha\right)^2 \tag{3}$$

$$\left|\vec{r}_0\right|\cos\alpha = \vec{r}_0 \cdot \boldsymbol{n_0} \tag{4}$$

where $\boldsymbol{n_0} = (\boldsymbol{u_0}, \boldsymbol{v_0}, \boldsymbol{w_0})$ is the unit vector along the gradient direction. The components of $\boldsymbol{n_0}$ are derived from the intensity magnitudes. For example, the x-component $(\boldsymbol{u_0})$ is calculated as,

$$u_0 = \frac{E_{-1} - E_1}{2v_x \left| \vec{\nabla} E_0 \right|} \tag{5}$$

where E_{-1} and E_1 are the intensities of neighboring voxels around point (x_0, y_0, z_0), $\left| \vec{\nabla} E_0 \right|$ is the gradient magnitude at the point (x_0, y_0, z_0), and v_x is the size of a voxel in the x-direction. Similar calculations apply for the y and z-directions, and Eq. (3) can be transformed to

$$d_0^{\,2} = \left(x_c - x_0 \right)^2 + \left(y_c - y_0 \right)^2 + \left(z_c - z_0 \right)^2 - \left[u_0 \left(x_c - x_0 \right) + v_0 \left(y_c - y_0 \right) + w_0 \left(z_c - z_0 \right) \right] \tag{6}$$

For a feature map that contains N gradient points, the cumulative distance (χ^2) from a candidate center point to all the gradient-parallel lines is calculated as,

$$\chi^2 = \sum_{k=1}^{N} d_k^{\,2} q_k \tag{7}$$

where q_k is a displacement weighting factor that reduces the impact of the elongation effects and enhances the robustness against noise. The weighting factor depends on the gradient magnitude and the distance from the point to the candidate center. According to Eq. (7), the particle center (x_c, y_c, z_c) is estimated by minimizing χ^2. This is achieved by setting the derivatives of χ^2 to zero and solving Eq. (8), which is

$$\begin{bmatrix} \sum\limits_{k=1}^{N}\left(1-u_0^{\,2}\right)q_k & -\sum\limits_{k=1}^{N}u_0 v_0 q_k & -\sum\limits_{k=1}^{N}u_0 w_0 q_k \\ -\sum\limits_{k=1}^{N}u_0 v_0 q_k & \sum\limits_{k=1}^{N}\left(1-v_0^{\,2}\right)q_k & -\sum\limits_{k=1}^{N}v_0 w_0 q_k \\ -\sum\limits_{k=1}^{N}u_0 w_0 q_k & -\sum\limits_{k=1}^{N}v_0 w_0 q_k & \sum\limits_{k=1}^{N}\left(1-w_0^{\,2}\right)q_k \end{bmatrix} \begin{bmatrix} x_c \\ y_c \\ z_c \end{bmatrix} = \begin{bmatrix} -\sum\limits_{k=1}^{N}\left[\left(u_0^{\,2}-1\right)q_k x_k + u_0 v_0 q_k y_k + u_0 w_0 q_k z_k\right] \\ -\sum\limits_{k=1}^{N}\left[\left(v_0^{\,2}-1\right)q_k y_k + u_0 v_0 q_k x_k + v_0 w_0 q_k z_k\right] \\ -\sum\limits_{k=1}^{N}\left[\left(w_0^{\,2}-1\right)q_k z_k + u_0 w_0 q_k x_k + v_0 w_0 q_k y_k\right] \end{bmatrix} \tag{8}$$

2.3 Topology feature particle matching

Particle matching involves identifying the same physical particles located at different spatial positions across dual frames. To minimize erroneous matches and spurious velocity vectors, we propose a topology-feature matching (TFM) approach that combines a predictor-corrector strategy. This method is implemented in two steps. Firstly, 3D cross-correlation analysis is conducted to produce a coarse motion predictor, and then topology feature descriptors are generated to link particles across different frames.
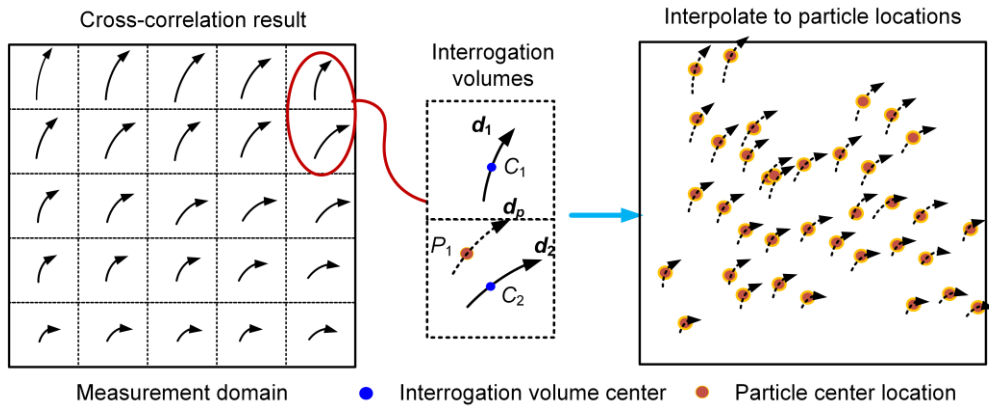

Fig. 5 Velocity interpolation from 3D motion predictor to each particle location.

To generate a motion predictor, the measurement domain is divided into smaller interrogation volumes, each containing several particles. The cross-correlation function is then computed in each interrogation volume based on the particle intensity distributions at two time instants. The correlation peak location indicates the average displacement of particle groups. Repeating this process over the entire domain yields a 3D displacement field with a uniform vector grid. The interrogation volumes are not overlapped, ensuring independence between generated displacement vectors. Due to the sparse nature of the

generated motion field, some particle positions may lack displacement vectors, particularly in densely seeded regions. Therefore, interpolations are performed to estimate the displacement at each particle location. Figure 5 provides the schematic of this interpolation operation. For an arbitrary point P_1, Euclidean distances to all interrogation volume centers are calculated, and the two nearest centers (C_1 and C_2) are identified. The displacement at point P_1 ($\boldsymbol{d_{pi}}$) is estimated as,

$$\boldsymbol{d_{pi}} = \begin{pmatrix} d_{pi,u} \\ d_{pi,v} \\ d_{pi,w} \end{pmatrix} = q_d \boldsymbol{d_{C_1}} + (1-q_d)\boldsymbol{d_{C_2}} = q_d \begin{pmatrix} d_{C_1,u} \\ d_{C_1,v} \\ d_{C_1,w} \end{pmatrix} + (1-q_d)\begin{pmatrix} d_{C_2,u} \\ d_{C_2,v} \\ d_{C_1,w} \end{pmatrix} \quad (9)$$

$$q_d = \frac{\|P_1 - C_2\|}{\|C_1 - C_2\|} \quad (10)$$

where $\boldsymbol{d_{C_1}}$ and $\boldsymbol{d_{C_2}}$ denotes the displacement at points C_1 and C_2, respectively, q_d is a weighting depends on the distance from P_1 to C_1, as defined in Eq. (10). Through this interpolation, the initial sparse displacement field is transformed into a denser one, assigning a unique displacement vector to each particle.

With the estimated particle local displacement, the particle center coordinates in the first frame (FR_1) are warped to new coordinates (FR_1', see Fig. 1). This warping operation ensures that particle displacements are smaller than the typical inter-particle separation distance, reducing the likelihood of incorrect particle pairings. A topology-feature-based approach is then utilized to match particles in FR_1' and FR_2. Unlike the NN method, the topology-feature-based approach leverages geometric relationships between particles. It utilizes the fact that particles close to one another in one frame should retain similar relative positions in subsequent frames.

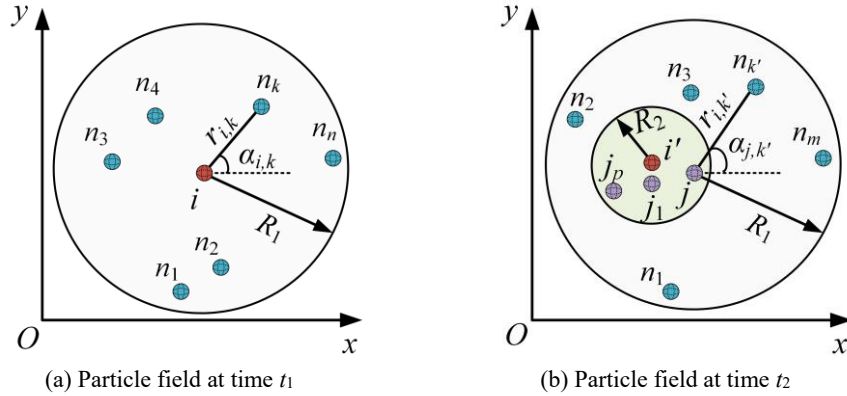(a) Particle field at time t_1 (b) Particle field at time t_2

Fig. 6 Schematic of topology-feature-based (TFM) approach for particle matching across dual frames.

The principle of the proposed TFM method is illustrated in Fig. 6. This figure shows a simplified 2D case for a clear illustration. In the first frame [Fig. 6(a)], within a search radius of R_1, the n-nearest neighboring particles ($n_1, n_2, \ldots, n_k, \ldots, n_n$) around the target particle (i) are identified. The local topology formed by particle i and a neighboring particle n_k is encoded into a geometry descriptor comprising two feature vectors: an angle-based feature ($\alpha_{i,k}$), defined as the angle between the line connecting two particles and the x-axis, and a distance feature ($r_{i,k}$) representing the Euclidean distance between the two particles. A total of n_n descriptors can be generated to describe the topology feature surrounding the particle i. In the second frame [Fig. 6(b)], if i' is a particle located at around i. Taking i' as the center and R_2 as the radius, candidate pairing particles of i ($j_1, \ldots, j, \ldots, j_p$) can be identified. For each candidate j, its m-nearest neighboring particles ($n_1, n_2, \ldots, n_{k'}, \ldots, n_m$) are found within the same search radius R_1, and corresponding topology descriptors ($\alpha_{i,k'}$ and $r_{i,k'}$) are generated. The similarity between the topology features of particles i and j are assessed by a similarity index ($s_{i,j}$), which quantifies differences in angle and distance features based on predefined thresholds (ε_{at} and ε_{rt}),

$$s_{i,j} = \sum\sum f(\varepsilon_a, \varepsilon_r) = \sum_k \sum_{k'} f\left(\varepsilon_{at} - \left|\alpha_{j,k'} - \alpha_{i,k}\right|, \varepsilon_{rt} - \left|r_{j,k'} - r_{i,k}\right|\right) \quad (11)$$

$$f\left(\varepsilon_a, \varepsilon_r\right) = \begin{cases} 1, & \varepsilon_a > 0, \varepsilon_r > 0 \\ 0, & \text{else} \end{cases} \tag{12}$$

where f is a step function defined in Eq. (12). According to Eqs. (11) and (12), similarity indices between i and j_1 to j_l are computed, and the candidate with the highest similarity index is selected as the most probable match for particle i. Repeating this process allows for tracking particle trajectories from the first frame to the second frame. For the 3D case, the matching process is analogous, the main difference is that the $\alpha_{i,k}$ also includes angles concerning the y and z-axes.

The displacements obtained by particle tracking ($\boldsymbol{d_{pt}}$) are then combined with the motion predictor ($\boldsymbol{d_{pi}}$) to form the final displacement field ($\boldsymbol{d_p}$),

$$\boldsymbol{d_p} = \begin{pmatrix} d_{p,u} \\ d_{p,v} \\ d_{p,w} \end{pmatrix} = \boldsymbol{d_{pi}} + \boldsymbol{d_{pt}} = \begin{pmatrix} d_{pi,u} \\ d_{pi,v} \\ d_{pi,v} \end{pmatrix} + \begin{pmatrix} d_{pt,u} \\ d_{pt,v} \\ d_{pt,w} \end{pmatrix} \tag{13}$$

Dividing $\boldsymbol{d_p}$ by the time interval between t_1 and t_2 yields a dense flow velocity field, containing the local velocity at each particle location.

3. Numerical verification

To assess the accuracy of the proposed method, numerical simulations are conducted using synthetic LFIs. The simulation begins with an idealized scenario in which the measurement domain contains a randomly distributed particle field, where each particle exhibits a radially symmetric intensity profile. This simulation offers the theoretical upper limit of accuracy achievable by the GF method, as it does not account for the particle location errors in volumetric reconstruction. Further analysis extended to the precision of particle center detection based on reconstructed particle fields through different methodologies. Specifically, the LoS-DNN method with a single LFC and the SMART algorithm using dual LFCs are employed. Finally, the proposed LF-PTV method was tested on synthetic Gaussian ring vortex data to evaluate its performance in measuring 3D displacement fields. The spatial resolution and accuracy of displacement measurements are compared across the conventional PIV and other PTV methods.

3.1 Particle localization accuracy

To generate a random particle field, a measurement volume with the physical dimensions of 14.1 mm × 14.1 mm × 14.1 mm is discretized into voxels with a spatial resolution of 0.1 mm × 0.1 mm × 0.1 mm along the x, y, and z-directions. Particles are randomly distributed in this volume, where voxel indices and intensities represent particles. The seeding density (C) is defined in particles per microlens (ppm) and varies from 0.1 ppm to 1 ppm. To model the elongation effect observed in the LF reconstructions, the intensity distribution of particles follows a modified Gaussian function,

$$E(x, y, z) = \exp\left(-\frac{8}{d_i}\left[(x - x_c)^2 + (y - y_c)^2 + \frac{(z - z_c)^2}{\alpha^2}\right]\right) \tag{14}$$

where $E(x, y, z)$ denotes the particle intensity at the location (x, y, z), (x_c, y_c, z_c) denotes the particle center location, d_i is the particle diameter (in voxel unit), and α is a scaling factor of d_i controlling the standard deviation in the z-direction. α leads to ellipsoidal intensity distributions, where the radii are d_i in the x and y-directions and αd_i in the z-direction. When $\alpha > 1$, particles are elongated into ellipsoids along z; when $\alpha < 1$, they are compressed.

The centers of seeded particles are detected through the GF method. For comparison, two commonly used methods, i.e., regional peak detection (RPD) and Laplacian of Gaussian (LoG) are also tested. RPD is a computationally efficient approach. It divides the entire image into several connection regions based on an intensity threshold and identifies the peak intensity location in each sub-region as the particle center. However, it may introduce artifacts in densely seeded regions. LoG is a slower but more robust method, which convolves the 3D image with a Gaussian filter, followed by the application of a Laplacian operator to identify particle centers. The results of particle center detection at $C = 0.1$ ppm are illustrated in Fig. 7, where gray dots represent correctly detected particles (TP, detected centers within 1 voxel chessboard distance of actual

particle centers), blue dots represent false negatives (FN, i.e., missed true particles) and red dots indicate false positives (FP, i.e., ghost particles erroneously identified). It can be observed that while all methods successfully detect most true particles, the GF method outperformed the others. RPD exhibit more false negatives and has a higher incidence of false positives. This outcome is likely due to RPD's reliance on the simple threshold in peak detection, which may introduce more detection artifacts in local dense seeding areas. The LoG method demonstrates greater robustness by combining Gaussian smoothing with the Laplacian operator, reducing false positives. However, it still does not achieve the same level of accuracy as the GF, which shows the fewest false positives among the three methods.

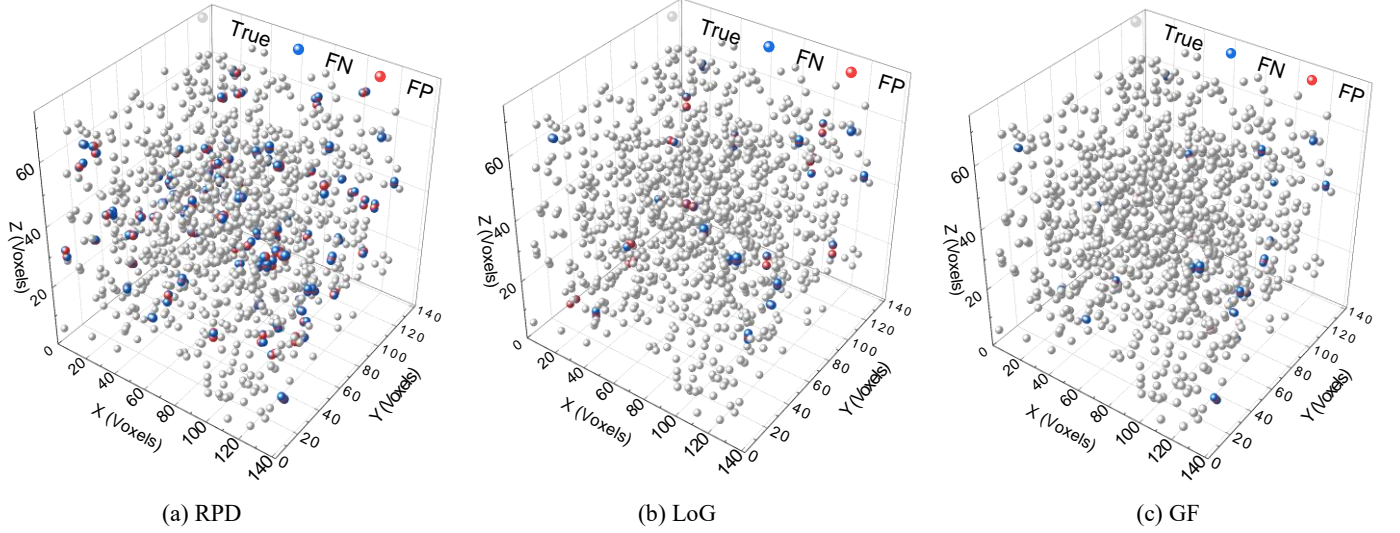(a) RPD   (b) LoG   (c) GF

Fig. 7 Particles detected by (a) regional peak detection (RPD), (b) Laplacian of Gaussian (LoG) and (c) gradient-based fitting (GF) methods. FN refers to the missed true particles, while FP refers to ghost particles erroneously identified.

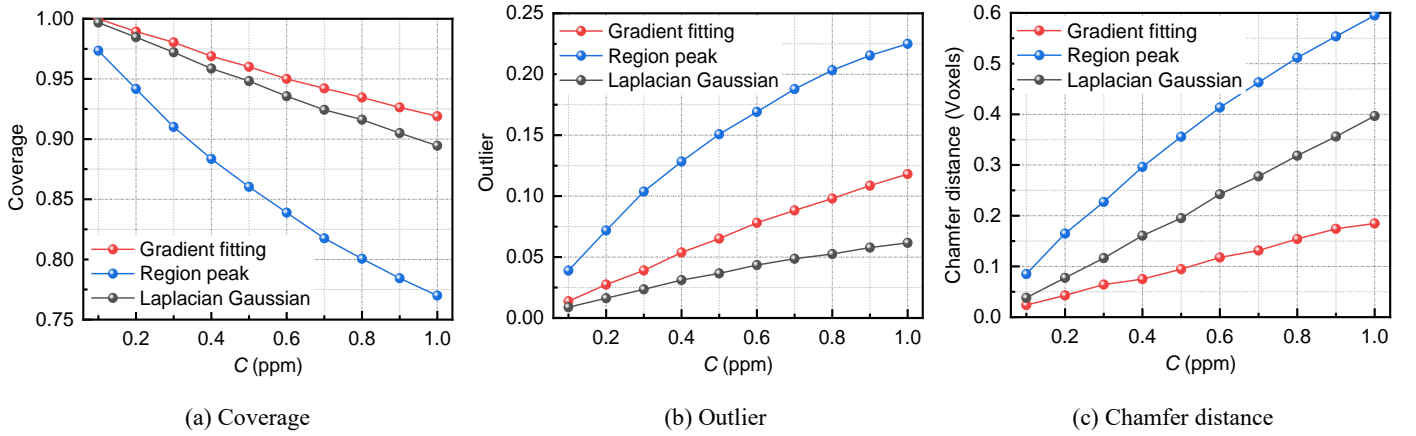(a) Coverage   (b) Outlier   (c) Chamfer distance

Fig. 8 Center detection accuracy by RPD, LoG and GF localization methods. The intensity distribution of each particle follows a modified Gaussian function [Eq. (15)]. The accuracy is assessed by (a) coverage, (b) outlier and (c) Chamfer distance.

The localization accuracy of PRD, LoG and GF is quantitatively evaluated using three metrics: coverage, outlier ratio, and Chamfer distance. The coverage quantifies the ratio of true particles successfully detected, serving as an indicator of precision in particle detection. The outlier ratio measures the proportion of ghost particles to the true particles, with lower values indicating higher accuracy in handling elongated particles. The Chamfer distance (d_C) compares two-point sets $A = \{a_1, a_2, \ldots a_m\}$ and $B = \{b_1, b_2, \ldots b_n\}$ in Euclidean space,

$$d_C(A, B) = \frac{1}{|A|} \sum_{a \in A} \min_{b \in B} \|a - b\| + \frac{1}{|B|} \sum_{b \in B} \min_{a \in A} \|b - a\| \tag{15}$$

Here, $\|a - b\|$ represents the Euclidean distance between points a and b, $\min_{b \in B} \|a - b\|$ denotes the nearest neighbor of a in set B, $\min_{a \in A} \|b - a\|$ denotes the nearest neighbor of b in set A, and $|A|$ and $|B|$ are the number of points in sets A and B, respectively.

According to Eq. (15), the Chamfer distance sums the average of the nearest-neighbor distances from each point in A to B and from each point in B to A. A smaller d_C indicates greater similarity between the two-point sets.

Figure 8 illustrates the performance of RPD, LoG and GF across different C based on these metrics. From Fig. 8(a), GF consistently achieves the highest coverage that maintains a value close to 1, hence indicating superior precision in detecting true particles. In contrast, RPD's coverage declines sharply as C increases, reflecting its reduced performance in denser particle fields. Figure. 8(b) reveals that LoG has the lowest outlier ratio across different C, effectively avoiding false particle detections. GF has a slightly higher outlier ratio than LoG, potentially because LoG's convolution step partially mitigates particle elongation. Figure 8(c) shows that GF has the smallest Chamfer distance across all C, indicating that the particle centers detected by GF are spatially closer to the true particle locations compared to RPD and LoG, therefore signifying GF's superior localization accuracy. Overall, results suggest that GF is a more effective method for detecting centers of elongated particles at dense seeding cases.

(a) Actual distribution

(b) LoS with single LFC

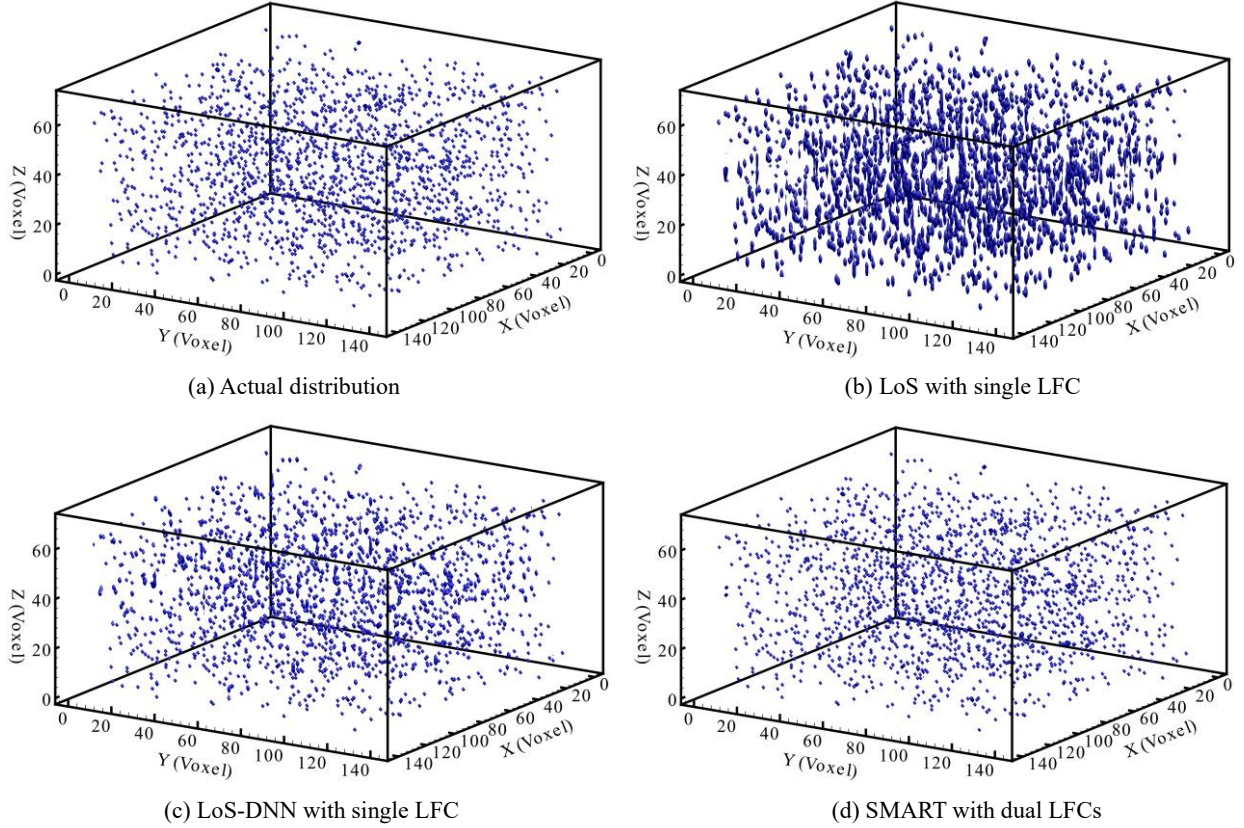(c) LoS-DNN with single LFC

(d) SMART with dual LFCs

Fig. 9 Random particle field at $C = 0.1$ ppm reconstructed by (b) LoS with single LFC, (c) LoS-DNN with single LFC, (d) SMART with dual LFCs, in comparison to (a) actual particle distribution.

The accuracy and robustness of the GF method are further examined on random particle fields numerically reconstructed from synthetic LFIs. To accomplish that, a dual LFC system with an angular separation of 90º is employed to generate synthetic LFIs of particle fields, as detailed in [19]. Both LFCs share identical optical parameters, as listed in Table. 1. To simulate practical noises and calibration errors, Gaussian white noise is integrated into the synthetic LFIs, following the methodology described in [39]. The reconstruction process began with a single LFC using the line-of-sight (LoS) estimation method, which was then refined with a deep neural network (DNN) model. For comparison, particle fields were also reconstructed using SMART with dual LFCs. The reconstructed particle fields by LoS and LoS-DNN with a single LFC and SMART with dual LFCs are subsequently processed with the GF method to localize particle centers.

Figure 9 presents the reconstructed random particle fields at $C = 0.1$ ppm using three algorithms, in comparison to the actual particle distribution [Fig. 9(a)]. The LoS estimation [Fig. 9(b)] captures an approximate particle distribution but suffers from elongations along the depth direction. Some elongated particles are fused, complicating accurate particle detection. The DNN-refined result [Fig. 9(c)] shows improvement over the basic LoS, with fewer elongated particles and distribution much

closer to the actual field, though minor clustering remains. The SMART algorithm with dual-LFCs [Fig. 9(d)] provides the most accurate reconstruction, closely resembling the actual distribution. Figure 10 illustrates the GF method's performance on reconstructed particle volumes across different C, assessed by coverage, outlier ratio, and Chamfer distance. It can be seen that the SMART with dual LFCs consistently achieves the highest coverage and lowest Chamfer distance across different C, whereas the LoS-DNN with a single LFC achieves the lowest outlier ratio. The basic LoS estimation, in contrast, demonstrates the lowest accuracy in dense particle fields. Due to the influence of reconstruction elongation and artificial noise, a decreased coverage, as well as a significantly larger outlier rate and Chamfer distance, are demonstrated in contrast to the ideal particle field (Fig. 8). Overall, while incorporating an additional LFC enhances the reconstruction and localization accuracy, the gains are modest relative to the increased experimental complexity. Through the use of LoS-DNN algorithm, a single LFC can achieve acceptable reconstruction accuracy, rendering it highly applicable in scenarios with limited optical access.

Table 1: Optical parameters of LFCs for synthetic LFIs generation

| Parameter	Symbol	Camera value
Magnification of the main lens	M	-1
Focal length of main lens	F_m	100 mm
f-number of main lens	$F/\#$	4
Focal length of microlens	f_m	800 μm
f-number of microlens	$f/\#$	8
Number of microlenses: x	n_m	250
Number of microlenses: y	n_n	250
Microlens pitch	p_m	100 μm
Camera resolution: x	n_x	6600
Camera resolution: y	n_y	4400
Pixel size	p_x	5.5 μm
Object focal distance	s_o	200 mm
Image distance	s_i	200 mm
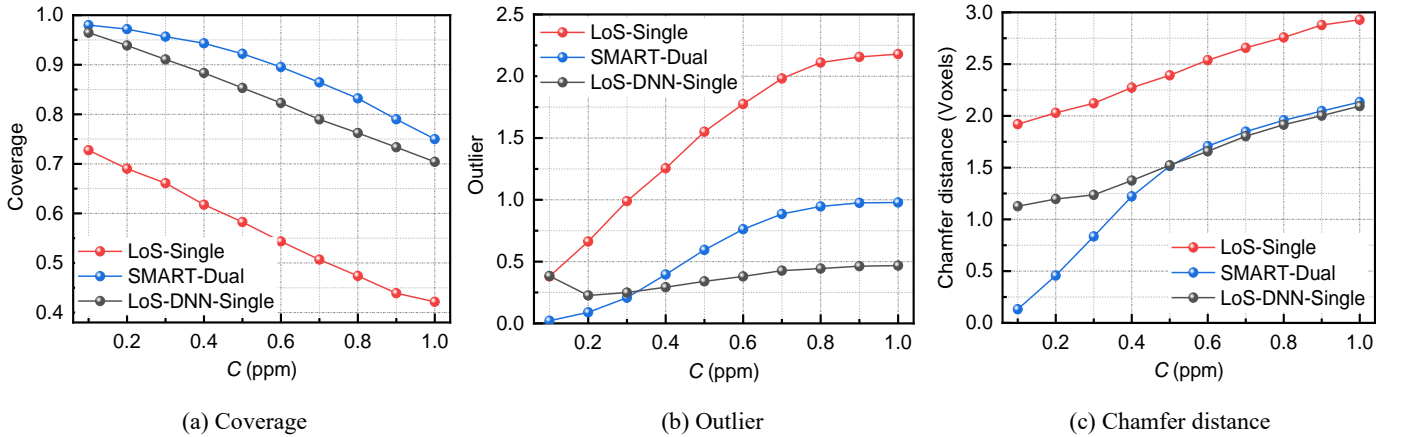
Fig. 10 Performance of the GF method on reconstructed particle fields by LoS and LoS-DNN methods with a single LFC, and SMART algorithm with dual LFCs. The performance is assessed by (a) coverage, (b) outlier and (c) Chamfer distance.

3.2 Displacement measurement accuracy

With the identified centers, particle matching between two successive frames is performed to estimate flow velocity. To evaluate the velocity measurement accuracy of the proposed TFM method, numerical tests are conducted on reconstructions of a synthetic Gaussian vortex field. Specifically, a synthetic displacement field representing a Gaussian ring vortex is applied to displace a random particle field to generate a displaced particle distribution. Synthetic LFIs for both the initial and displaced particle fields are generated with the LFC parameters detailed in Section 3.1. The analytical expression of the ring vortex and the vortex parameter settings are detailed in [19]. The vortex center is positioned at the center of the measurement volume, with the maximum particle displacement in the x, y, and z-directions set to 7.8 voxels. The particle fields are reconstructed

using the LoS-DNN algorithm and processed by the TFM method to obtain the displacement field. For comparison, three commonly used particle tracking approaches, the NN [49], relaxation matching algorithm (RM) [50], and augmented Lagrangian regularization method (LR) [2], are also employed. The particle displacements obtained from these methods were compared against the local displacement derived from the analytical solution of the ring vortex to assess the measurement accuracy.

In PTV, the tracking ratio serves as a key metric for evaluating the effectiveness of particle tracking methods. It quantifies the percentage of particles successfully tracked across sequential frames, with higher values indicating greater accuracy. Figure 11 compares the tracking ratio of different tracking methods under conditions with and without the use of a motion predictor. It can be observed that TFM consistently outperforms the other methods, maintaining a higher tracking ratio across the entire concentration range. This suggests that TFM is more effective at accurately tracking particles, even as seeding density increases. Without the motion predictor [Fig. 11(a)], all methods show a gradual decrease in tracking ratio as C increases, indicating that dense seeding makes tracking more challenging. However, when the motion predictor is employed [Fig. 11(b)], all methods exhibit improved tracking ratios, particularly at higher C. This improvement is more significant for TFM and RM, which suggests that the motion predictor helps reduce the likelihood of mismatches in particle trajectories. Overall, the results demonstrate that TFM combined with a motion predictor yields the most robust tracking performance.

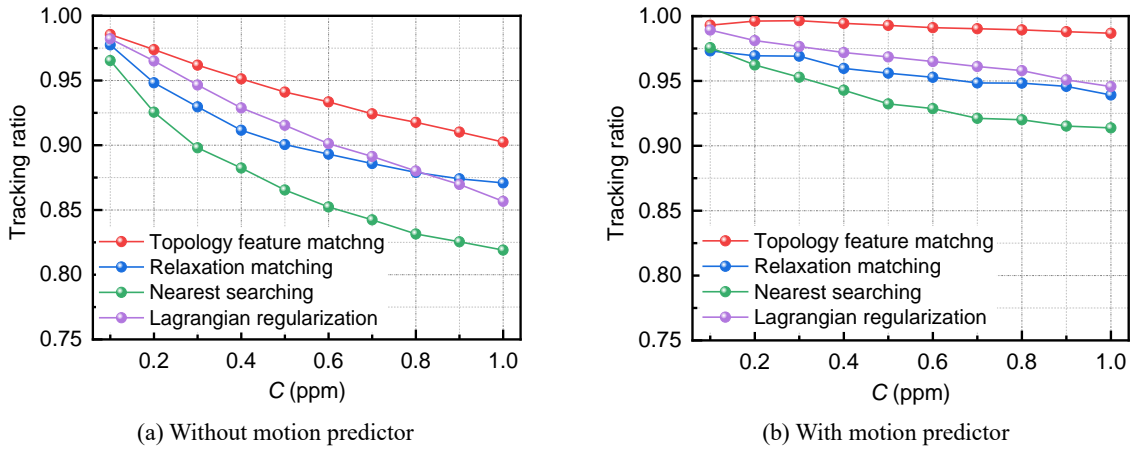(a) Without motion predictor (b) With motion predictor

Fig. 11 Particle tracking ratio of different tracking methods (a) without using particle motion predictor and (b) using the predictor.

Figure 12 shows the 3D displacement field of the ring vortex reconstructed by PIV, TFM-based PTV and NN-based PTV at $C = 0.2$ ppm and 0.8 ppm. The result indicates that at both C levels, the TFM-based PTV method produces a more cohesive and consistent representation of the vortex structure, with denser particle distributions and clearer flow patterns compared to the other methods. In contrast, the PIV method shows sparser particle trajectories and reduced spatial resolution in the vortex core region, which remains unsolved even at high seeding densities. While the NN-based PTV achieves comparable accuracy with TFM-based PTV at $C = 0.2$ ppm, its accuracy deteriorates significantly as C increases. The elevated particle density leads to a higher incidence of erroneous particle matches, resulting in spurious vectors that distort the vortex structure. These findings underscore the robustness of the TFM-based method in reconstructing detailed vortex dynamics, particularly under dense particle density conditions.

Quantitative evaluations of the TFM-based PTV are conducted in terms of displacement measurement accuracy and spatial resolution. The accuracy is quantified by the root mean square error (RMSE) of the reconstructed displacement field, defined as

$$RMSE = \sqrt{\frac{1}{n_{vec}} \sum_{i=1}^{n_{vec}} \left(\boldsymbol{d}_p - \boldsymbol{d}_t \right)^2} \tag{16}$$

where $\boldsymbol{d}_p$ and $\boldsymbol{d}_t$ are the estimated and true displacement, respectively, n_{vec} denotes the number of independent displacement vectors returned by the PIV or PTV algorithms. The spatial resolution is quantified by the mean vector spacing (sp_v) calculated as,

$$sp_v = \sqrt[3]{\frac{3V}{4\pi n_{vec}}} \qquad (17)$$

where V is the volume of measurement domain in units of mm³. A smaller sp_v with signifies a denser vector field and therefore higher spatial resolution.

(a) PIV, $C = 0.2$ ppm

(b) PIV, $C = 0.8$ ppm

(c) TFM-based PTV, $C = 0.2$ ppm

(d) TFM-based PTV, $C = 0.8$ ppm

(e) NN-based PTV, $C = 0.2$ ppm
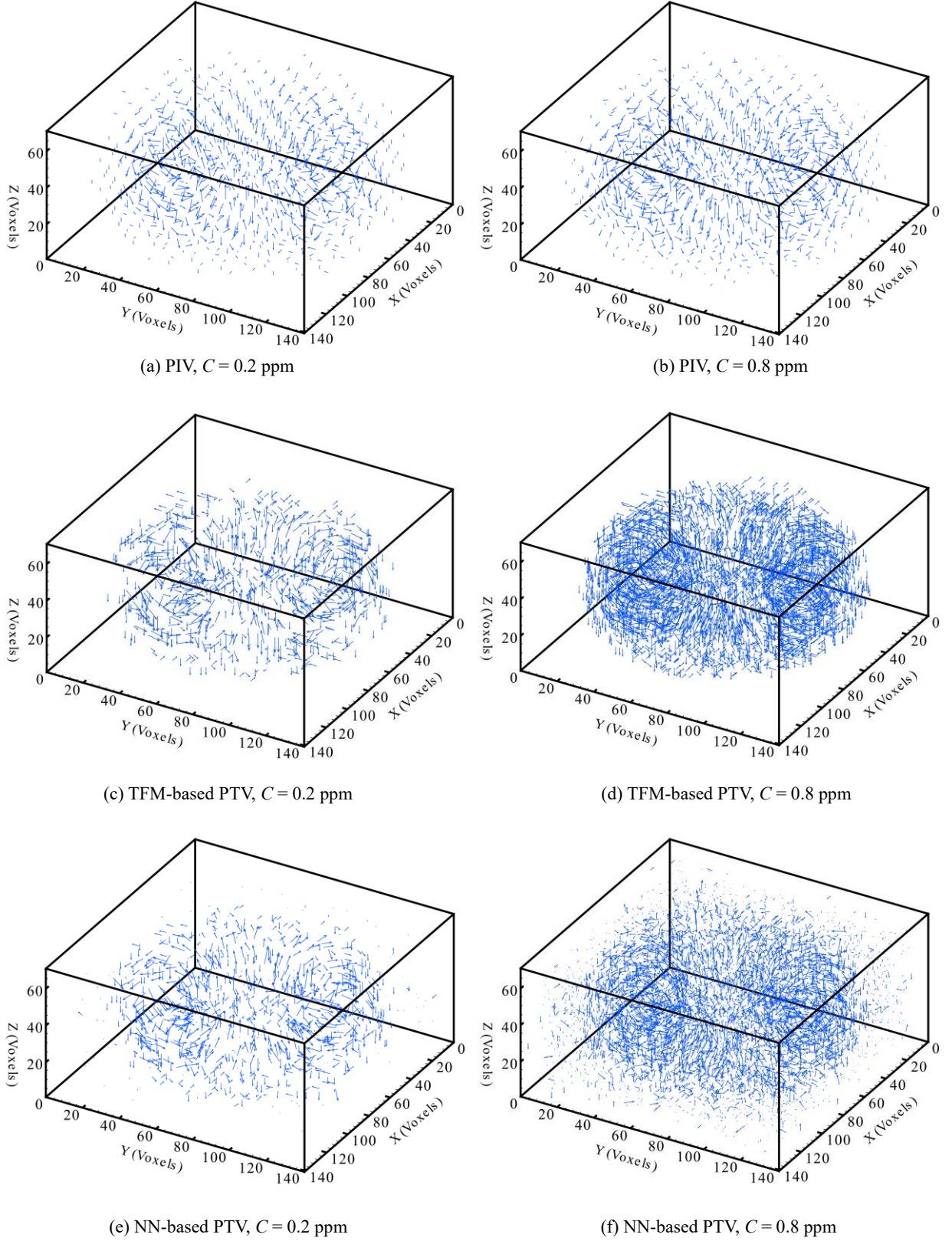
(f) NN-based PTV, $C = 0.8$ ppm

Fig. 12 Comparison of reconstructed 3D displacement field of the ring vortex by (a) and (b) PIV algorithm, (c) and (d) TFM-based PTV, and (e) and (f) NN-based PTV. The particle fields at $C = 0.2$ and 0.8 ppm are reconstructed by the LoS-DNN algorithm using a single LFC.

16

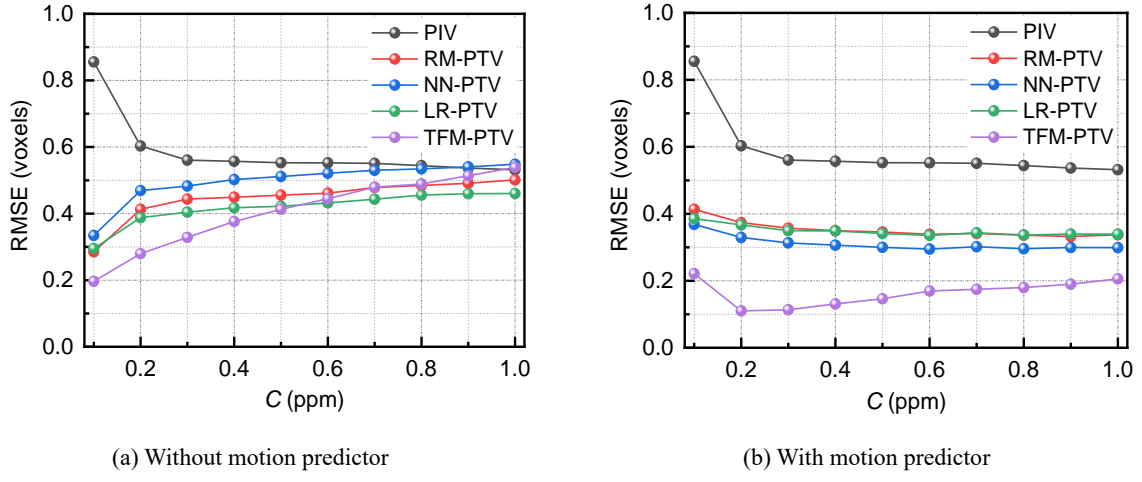| (a) Without motion predictor | (b) With motion predictor |

Fig. 13 RMSE of displacement field of the ring vortex reconstructed by different methods (a) without using particle motion predictor and (b) using the predictor.

Figure 13 depicts the RMSE of the displacement field reconstruction using different particle tracking methods with and without a particle motion predictor. The results indicate that without the predictor, the RMSE generally decreases with increasing C, stabilizing beyond 0.4 ppm for most methods. The PIV method shows the highest RMSE, indicating the lowest accuracy, particularly at lower C. In contrast, when the motion predictor is combined, there is a noticeable decrease in RMSE for all methods. Overall, TFM-based PTV consistently maintains its superior performance with the lowest RMSE across all C, further demonstrating its effectiveness when combined with motion predictor. Figure 14 illustrates the sp_v of different methods with varying C. For traditional PIV, sp_v decreases significantly as the interrogation volume size (I_v) decreases, indicating enhanced spatial resolution with finer volumes. In contrast, PTV methods exhibit higher spatial resolution than PIV. sp_v decreases with increasing C for all methods, demonstrating improved spatial resolution with higher C. Among these methods, TFM-based PTV consistently achieves the lowest sp_v across the tested C range. This result highlights the effectiveness of the TFM approach in achieving high spatial resolution in dense particle tracking scenarios, outperforming traditional methods.

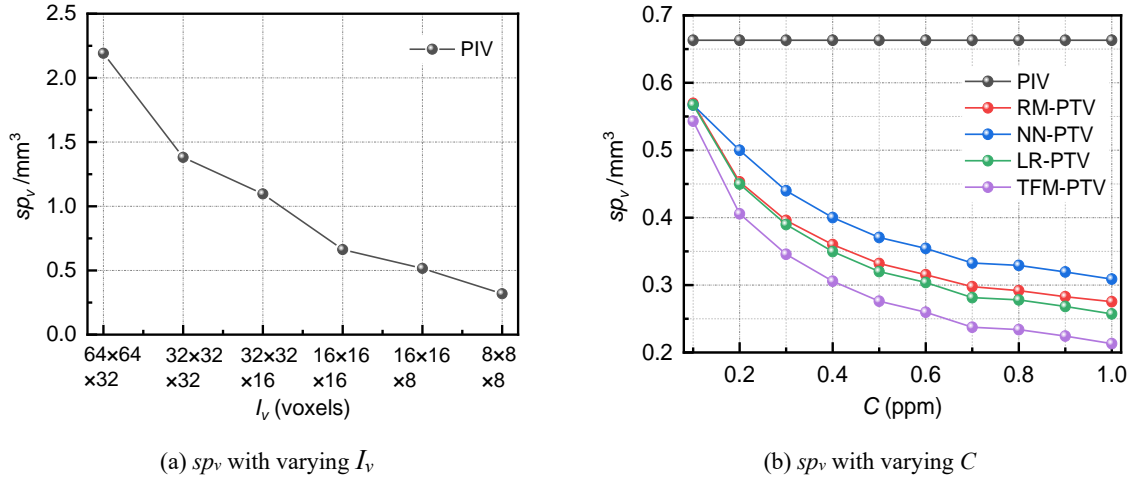| (a) sp_v with varying I_v | (b) sp_v with varying C |

Fig. 14 Mean vector spacing sp_v in vortex displacement field reconstruction by different methods. (a) and (b) shows variations of sp_v with interrogation volume size I_v and seeding density C, respectively.

4. Experimental validation

The proposed LF-PTV method is further validated through experimental measurements of the 3D wake flow around a circular cylinder. The experimental setup is schematically illustrated in Fig. 15. Water flow within a glass channel (cross-section of 2 cm × 2 cm) is driven by a metering pump, maintaining steady flow rates (Q) of 70 L/h and 100 L/h, respectively.

The flow rate is monitored via a flowmeter and controlled by a PID controller to ensure a stable laminar flow in the fully developed region of the channel. A circular cylinder with a diameter (d) of 2 mm is positioned in this region to facilitate the measurement of the 3D velocity field of the wake flow. Polyamide particles, seeded at a density of approximately 0.6 ppm, are used as tracers for flow visualization. Volume illumination is provided by a double-pulse laser coupled with a beam expander, delivering a peak energy of 200 mJ at a wavelength of 532 nm, with each pulse lasting approximately 7 ns. A customized LFC, with a pixel resolution of 2352 (H)×1768 (V), is utilized to capture the LFIs of particle motion. Optical parameters of the LFC are kept consistent with those used in the simulations (Table 1), enabling a measurement volume of approximately $5d \times 6.5d \times 6d$ in the x, y and z directions, respectively.
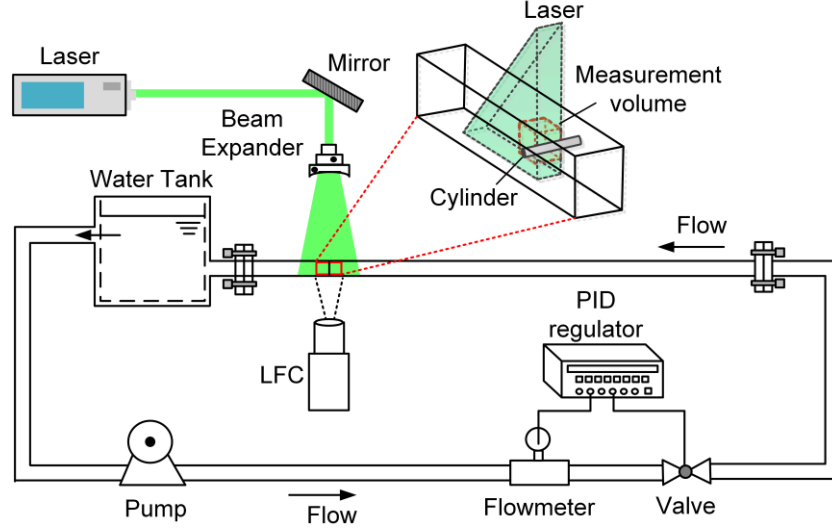

Fig. 15 Schematic of the experimental setup of the wake flow around a circular cylinder.

The recorded LFIs are analyzed with the LF-PTV method to estimate flow velocity. Initially, the LoS estimation generates a coarse particle distribution, followed by DNN refinement to resolve the particle elongation issue. Particle centers in two reconstructed volumes were identified using the GF algorithm, and particle pairing across successive frames was achieved through the TFM method. To benchmark the performance of the proposed method, comparative measurements were conducted using the conventional LF-PIV. In the LF-PIV, particle volumes were reconstructed via the SMART algorithm with a single LFC, followed by a cross-correlation analysis to estimate the velocity field. The interrogation volume size is set to 16×16×16 voxels with a 50% overlap. A total of 250 instantaneous velocity fields reconstructed by LF-PTV and LF-PIV are collected to provide statistical insights into the cylinder wake flow.

In the PIV estimation, the returned velocity vectors in each instantaneous flow field are fixed at the centers of interrogation volumes. By averaging the velocity values within each interrogation window over time, a mean flow field can be acquired. In contrast, the PTV algorithm provides a local velocity field at the positions of tracer particles, which vary as particles move with the flow. The mean velocity $\bar{V}_{x,y,z}$ at particle location (x, y, z) obtained by PTV can be calculated as

$$\bar{V}_{x,y,z} = \frac{\sum_{i=1}^{n} V_{x,y,z,i}}{n} \tag{18}$$

where n denotes the number of acquired velocity vectors at the current location across all instantaneous flow fields.

Figure 16 presents the mean velocity fields of the 3D cylinder wake flow, comparing the LF-PIV and LF-PTV methods at $Q = 70$ L/h and 100 L/h. Figures 16(a) and (c) display results from the conventional LF-PIV method, while Figs. 16(b) and (d) correspond to the proposed LF-PTV method. At different Q, the LF-PIV results present smoother, more averaged flow fields, reflecting the method's reliance on fixed interrogation volumes for estimating mean flow. In contrast, the LF-PTV method provides a more detailed depiction of the local flow at tracer particle positions, highlighting variations in flow velocity more effectively. Additionally, the LF-PTV method captures finer fluctuations and smaller eddy structures, which may be lost in the coarser LF-PIV analysis. The contours represent the magnitude of the streamwise velocity component (v), revealing a

18

similar pattern in overall flow distribution across both methods, though LF-PTV displays greater detail. Similar findings can also be observed in the reconstructed instantaneous velocity field.
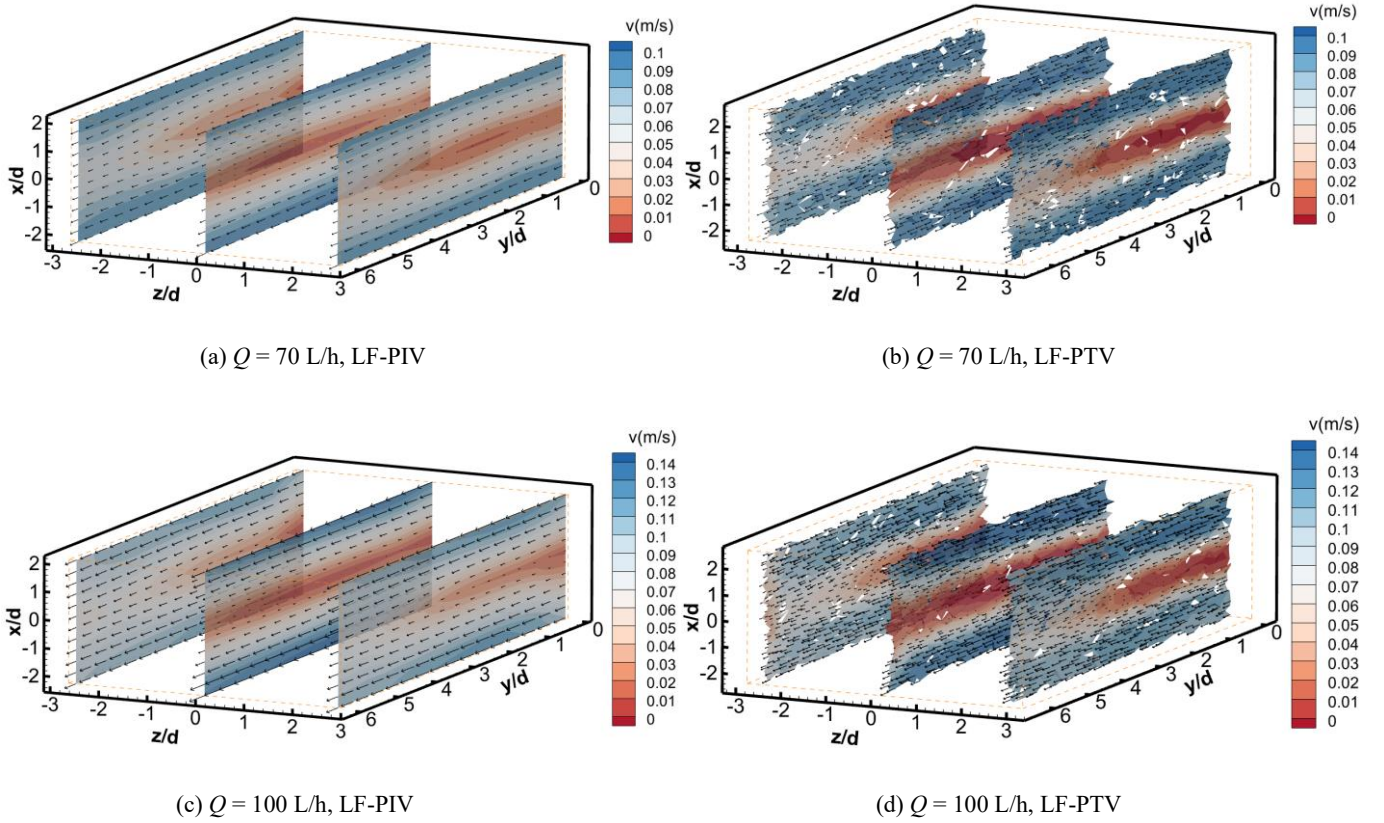

(a) $Q = 70$ L/h, LF-PIV

(b) $Q = 70$ L/h, LF-PTV

(c) $Q = 100$ L/h, LF-PIV

(d) $Q = 100$ L/h, LF-PTV

Fig. 16 Mean velocity field of 3D wake flow of a cylinder at $Q = 100$ L/h and 70 L/h measured by (a) and (c) the low-resolution LF-PIV technique, as well as (b) and (d) the proposed high-resolution LF-PTV method.

Figure 17 presents 2D slices at central depth of the channel, which are extracted from 3D wake flow velocity data. The LF-PTV method consistently demonstrates finer details in the wake flow structure behind the cylinder, capturing more distinct vortex patterns compared to the smoother, more averaged structures observed in the LF-PIV measurements. The magnified insets further emphasize the difference, showing that LF-PTV reveals sharper, more localized flow features and smaller-scale eddies, particularly near the cylinder wake region. This observation suggests that LF-PTV offers enhanced spatial resolution and captures transient flow structures more effectively than LF-PIV, which could be beneficial for detailed flow studies in complex geometries. Both methods, however, depict similar large-scale flow patterns, confirming their consistency in capturing the general wake flow behavior. According to Eq. (17), the sp_v of LF-PIV and LF-PTV in cylinder wake flow measurements is 0.61 and 0.21, respectively, indicating that the spatial resolution of LF-PTV improves by approximately threefold compared to the conventional PIV algorithm.

(a) Q = 70 L/h, LF-PIV

(b) Q = 70 L/h, LF-PTV
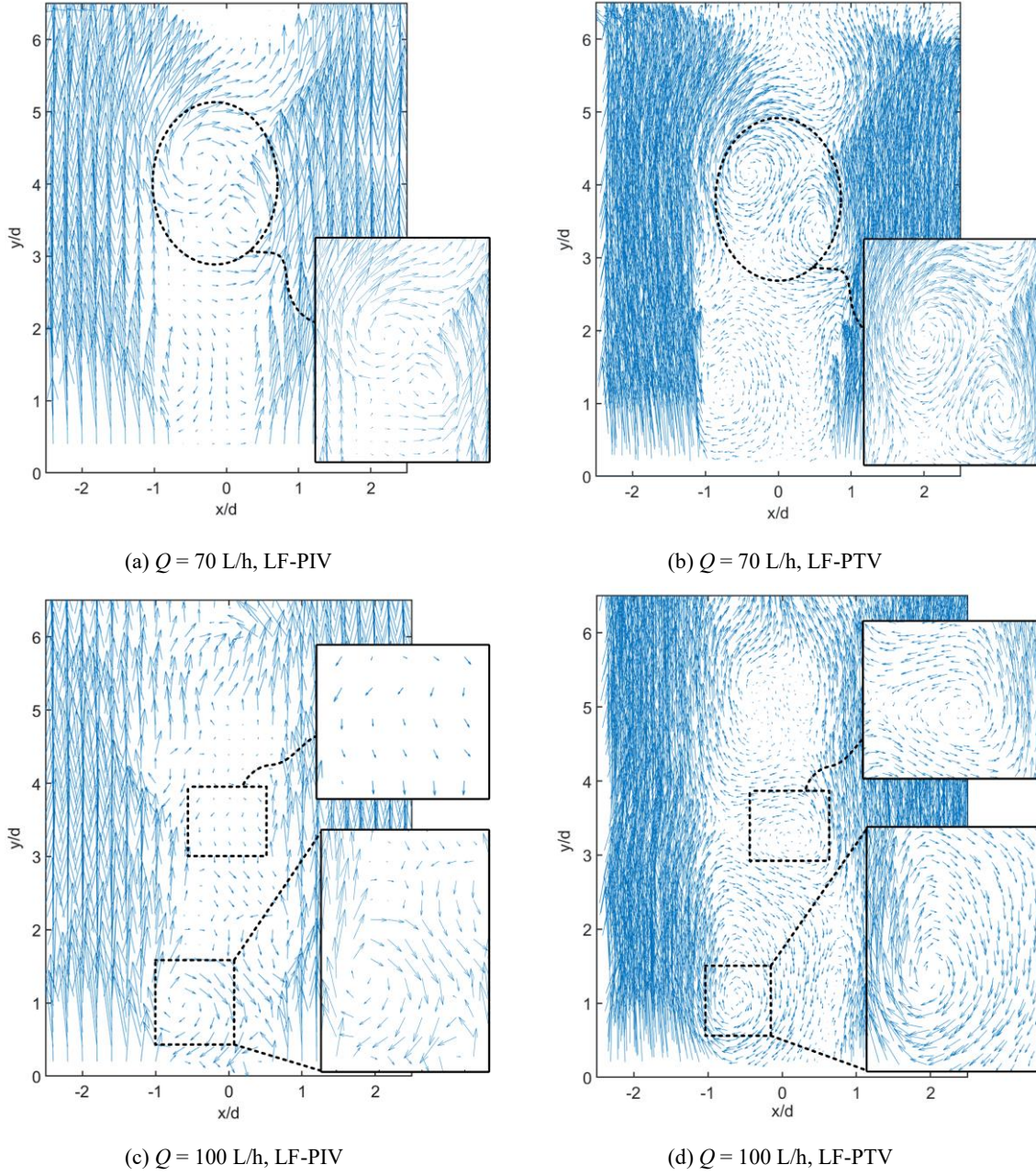
(c) Q = 100 L/h, LF-PIV

(d) Q = 100 L/h, LF-PTV

Fig. 17 2D slices at central depth plane extracted from 3D flow data, showing the instantaneous velocity vectors measured by conventional LF-PIV and proposed LF-PTV methods.

5. Conclusion

This study introduces a high-resolution dual-frame LF-PTV approach for resolving fine structures in 3D unsteady flows. A customized deep neural network (DNN) is employed to refine the coarse 3D particle distribution initially estimated via the line-of-sight (LoS) technique. Particle localization is performed using a gradient-based fitting (GF) localization algorithm, followed by particle tracing through the topology-feature matching (TFM) method. Comparative evaluations with alternative PTV methods and the conventional LF-PIV technique are conducted using synthetic and experimental data. The key findings are summarized as follows:

- The DNN approach effectively mitigates particle elongation demonstrated in LoS estimation. The DNN reconstruction with a single LFC achieves approximate accuracy to the traditional SMART algorithm utilizing dual LFCs.
- The GF algorithm outperforms traditional localization approaches in handling elongated particles, delivering higher coverage rates with fewer outliers, particularly in densely seeded scenarios.
- Integrating the TFM method with a motion predictor minimizes particle mismatches in particle tracking, achieving the

lowest root mean square error and mean vector spacing in synthetic Gaussian vortex field reconstructions.

- LF-PTV captures finer details of the wake flow structure around a cylinder, resolving more distinct vortex patterns compared to the smoother, more averaged structures observed in LF-PIV measurements. Additionally, LF-PTV effectively corrects erroneous vectors in LF-PIV results, achieving approximately a threefold enhancement in spatial resolution.

To further deepen the understanding of unsteady complex flow structures, future work will aim to integrate high-resolution dense flow data with physical constraints (e.g., Navier-Stokes equations) to enhance temporal resolution in LF-PTV measurements.

Author Declaration

Conflict of interest

The authors declare that they have no known competing financial interests or personal relationships that could have appeared to influence the work reported in this paper.

Acknowledgements

References

[1] Westerweel J, Elsinga G E, Adrian R J. Particle image velocimetry for complex and turbulent flows[J]. Annual Review of Fluid Mechanics, 2013, 45: 409-436.

[2] Schröder A, Schanz D. 3D Lagrangian particle tracking in fluid mechanics[J]. Annual Review of Fluid Mechanics, 2023, 55: 511-540.

[3] Scarano F. Tomographic PIV: principles and practice[J]. Measurement Science and Technology, 2013, 24(10): 012001.

[4] Crane R J, Popinhak A R, Martinuzzi R J, et al. Tomographic PIV investigation of vortex shedding topology for a cantilevered circular cylinder[J]. Journal of Fluid Mechanics, 2022, 931: R1.

[5] She W, Gao Q, Zuo Z, et al. Experimental study on a zigzagging bubble using tomographic particle image velocimetry with shadow image reconstruction[J]. Physics of Fluids, 2021, 33(8): 083313.

[6] Qu Q, Cao Z, Xu L, et al. Reconstruction of two-dimensional velocity distribution in scramjet by laser absorption spectroscopy tomography[J]. Applied Optics, 2019, 58: 205-212.

[7] Cheng H, Ji B, Long X, et al. A review of cavitation in tip-leakage flow and its control[J]. Journal of Hydrodynamics, 2021, 33(2): 226-242.

[8] Zhao Z, Ding J, Shi S, et al. Volumetric flow characterization of a rectangular orifice impinging synthetic jet with single-camera light-field PIV[J]. Experimental Thermal and Fluid Science, 2021, 123(5), 110327.

[9] Zhu X, Xu C, Hossain M M, et al. Approach to select optimal cross-correlation parameters for light field particle image velocimetry[J]. Physics of Fluids, 2022, 34(7): 073601.

[10] Cao L, Zhang B, Hossain M M, et al. Tomographic reconstruction of light field PIV based on a backward ray tracing technique [J]. Measurement Science and Technology, 2021, 32: 044007.

[11] Thomas L, Trembiais B, David L. Optimization of volume reconstruction for classical Tomo-PIV algorithms (MART, BIMART and SMART): synthetic and experimental studies[J]. Measurement Science and Technology, 2014, 25(2): 035303.

[12] Xing F, Wang D, Tan H, et al. High-resolution light-field particle imaging velocimetry with color-and-depth encoded illumination[J]. Optics and Lasers in Engineering, 2024, 173: 107921.

[13] Deem E A, Zhang Y, Cattafesta L N, et al. On the resolution of plenoptic PIV[J]. Measurement Science and Technology, 2016, 27: 084003.

[14] Toloui M, Hong J. High fidelity digital inline holographic method for 3D flow measurements[J]. Optics Express, 2015, 23(21): 27159-27173.

[15] Shi S, Ding J, New TH, et al. Light-field camera-based 3D volumetric particle image velocimetry with dense ray tracing reconstruction technique[J]. Experiments in Fluids, 2017, 58: 78.

[16] Zhu X, Wu Z, Li J, et al. A pre-recognition SART algorithm for the volumetric reconstruction of the light field PIV[J]. Optics and Lasers in Engineering, 2021, 143: 106625.

[17] Discetti S, Natale A, Astarita T. Spatial filtering improved tomographic PIV[J]. Experiments in Fluids, 2013, 54: 1505.

[18] Mei D, Ding J, Shi S, et al. High resolution volumetric dual-camera light-field PIV[J]. Experiments in Fluids, 2019, 60: 132.

[19] Zhu X, Xu C, Hossain M M, et al. Fast and accurate flow measurement through dual-camera light field particle image velocimetry and ordered-subset algorithm[J]. Physics of Fluids, 2023, 35(6): 63603.

[20] Worth N A, Nickels T B. Acceleration of Tomo-PIV by estimating the initial volume intensity distribution[J]. Experiments in Fluids, 2008, 45(5): 847-856.

[21] Atkinson C, Soria J. An efficient simultaneous reconstruction technique for tomographic particle image velocimetry[J]. Experiments in Fluids, 2009, 47: 553-568.

[22] Zeng X, He C, Liu Y. GPU-accelerated MART and concurrent cross-correlation for tomographic PIV[J]. Experiments in Fluids, 2022, 63: 91.

[23] Wang G, Ye J C, Man B D. Deep learning for tomographic image reconstruction[J]. Nature Machine Intelligence, 2020, 2: 737-748.

[24] Shimobaba T, Takahashi T, Yamamoto Y, et al. Digital holographic particle volume reconstruction using a deep neural network[J]. Applied Optics, 2019, 58(8): 1900-1906.

[25] Barnkob R, Cierpka C, Chen M, et al. Defocus particle tracking: a comparison of methods based on model functions, cross-correlation, and neural networks[J]. Measurement Science and Technology, 2021, 32(9): 094011.

[26] Gim Y, Jang D K, Sohn D K, et al. Three-dimensional particle tracing velocimetry using shallow neural network for real-time analysis[J]. Experiments in Fluids, 2020, 61: 26.

[27] Himpel M, Melzer A. Fast 3D particle reconstruction using a convolutional neural network: application to dusty plasmas[J]. Machine Learning: Science and Technology, 2021, 2(4): 045019.

[28] Gao Q, Pan S, Wang H, et al. Particle reconstruction of volumetric particle image velocimetry with the strategy of machine learning[J]. Advances in Aerodynamics, 2021, 3(9): 28.

[29] Liang J, Cai S, Xu C, et al. Filtering enhanced tomographic PIV reconstruction based on deep neural networks[J]. IET Cyber-Systems and Robotics, 2020, 2(1): 43-52.

[30] Shao S, Mallery K, Kumar S S, et al. Machine learning holography for 3D particle field imaging[J]. Optics Express, 2020, 28(3): 2987-2999.

[31] Shao S, Mallery K, Hong J, et al. Machine learning holography for measuring 3D particle distribution[J]. Chemical Engineering Science, 2020, 225(11): 115830.

[32] Chen N, Wang C, Heidrich W. Holographic 3D particle imaging with model-based deep network[J]. IEEE Transactions on Computational Imaging, 2021, 7(3): 288-296.

[33] Herman G T, Lent A. Iterative reconstruction algorithms[J]. Computers in Biology and Medicine, 1976, 6(4): 273-294.

[34] Baldi P. Gradient descent learning algorithm overview: a general dynamical systems perspective[J]. IEEE Transactions on Neural Network, 1995, 6(1): 182-195.

[35] Sze V, Chen H, Yang J, et al. Efficient processing of deep neural networks: A tutorial and survey[J]. Proceedings of the IEEE, 2017, 105(12): 2295-2329.

[36] Li Z, Liu F, Yang W, et al. A survey of convolutional neural networks: analysis, applications, and prospects[J]. IEEE Transactions on Neural Networks and Learning, 2022, 33(12): 6999-7019.

[37] Liu W, Wang Z, Liu X, et al. A survey of deep neural network architectures and their applications[J]. Neuro computing, 2017, 234: 11-26.

[38] He, K, Zhang, X, Ren, S, et al. Deep Residual Learning for Image Recognition[C]. In Proceedings of the 2016 IEEE Conference on Computer Vision and Pattern Recognition (CVPR), Las Vegas, USA, 2016, 770–778.

[39] Cai S, Zhou S, Xu C, et al. Dense motion estimation of particle images via a convolutional neural network[J]. Experiments in Fluids, 2019, 60: 73.

[40] Cai S, Liang J, Gao Q, et al. Particle image velocimetry based on a deep learning motion estimator[J]. IEEE Transactions on Instrumentation and Measurement, 2020, 69(6): 3538-3554.

[41] Chen H, Wang M, Zhao X. A multi-strategy enhanced sine cosine algorithm for global optimization and constrained practical engineering problems[J]. Applied Mathematics and Computation, 2020, 369: 124872.

[42] Kingma D, Ba J. Adam: a method for stochastic optimization[C]. In Proceedings of the 3rd international conference on learning representations (ICLR), 2014.

[43] He L, Chao Y, Suzuki K, et al. Fast connected-component labeling[J]. Pattern Recognition, 2009, 42(9): 1977-1987.

[44] Wang Z, Bovcik A C, Sheikh H R, et al. Image quality assessment: from error visibility to structural similarity[J]. IEEE Transactions on Image Processing, 2004, 13(4): 600-612.

[45] Zhu X, Hossain M M, Li J, et al. Weight coefficient calculation through equivalent ray tracing method for light field particle image velocimetry[J]. Measurement, 2022, 193: 110982.

[46] Shi S, Ding J, New T H, et al. Volumetric calibration enhancements for single-camera light-field PIV[J]. Experiments in Fluids, 2019, 60: 1-16.

[47] Yu C, Bi X, Fan Y. Deep learning for fluid velocity field estimation: A review[J]. Ocean Engineering, 2023, 271(3): 113693.

[48] Yu C, Fan Y W, Bi X, et al. Deep dual recurrence optical flow learning for time-resolved particle image velocimetry[J]. Physics of Fluids, 2023, 35(4): 045104.

[49] Pereira F, Stuer H, Graff E C, et al. Two-frame 3D particle tracking[J]. Measurement Science and Technology, 2006, 17(7): 1680.

[50] Brevis W, Nino Y, Jirka G H. Integrating cross-correlation and relaxation algorithms for particle tracking velocimetry[J]. Experiments in Fluids, 2011, 50: 135-147.